

Injection Locking at Fractional Frequencies of Magnetic-Tunnel-Junction-Based Read Sensors' Ferromagnetic Resonance Modes


Ekaterina Auerbach^{1,*}, Dmitry Berkov^{2,†}, Bernhard Pichler,³ Norbert Leder,³ Holger Arthaber,³ and Savas Gider⁴

¹*Institute of Solid-State Physics, Vienna University of Technology, Vienna 1040, Austria*

²*General Numerics Research Lab e.V., Moritz-von-Rohr-Straße 1A, Jena 07745, Germany*

³*Institute of Electrodynamics, Microwave and Circuit Engineering, Vienna University of Technology, Vienna 1040, Austria*

⁴*Western Digital Corporation, San Jose, California 95119, USA*

 (Received 18 May 2019; revised manuscript received 25 August 2019; published 8 November 2019; corrected 19 December 2019)

Being nonlinear dynamic systems, magnetic read sensors should respond to an excitation signal of a frequency considerably different from their natural ferromagnetic resonance (FMR) frequencies. Because of the magnetization dynamics' inherent nonlinear nature, the sensors' response should be measured at the dc, excitation frequency, and its multiples (harmonics). In this paper, we present results of such measurements, accomplished using a one-port nonlinear vector network analyzer (NVNA), which show distinct resonances at fractional frequencies of the free layer (FL) FMR mode. Identification of these resonances, resulting from the nonlinear nature of the spin-torque (ST)-induced magnetization dynamics, is performed using micromagnetic modeling. In particular, we show that the measured dc response at the above-mentioned fractional frequencies can be explained by a low-order nonlinearity and strong magnetodipolar feedback between magnetic layers adjacent to a MgO barrier. Additionally, we determine that the simulated harmonic response is strongly enhanced by the mutual ST effect between these layers. Finally, we demonstrate that the read sensors' nonlinear magnetization dynamics and, by extension, their harmonic response are highly sensitive to various magnetic and ST parameters. Thus, this study shows that using NVNA measurements in conjunction with micromagnetic modeling can clarify the uncertainty in the definition of these parameters.

DOI: [10.1103/PhysRevApplied.12.054022](https://doi.org/10.1103/PhysRevApplied.12.054022)

I. INTRODUCTION

A magnetic tunnel junction (MTJ) is the basis of modern read sensors commonly used in hard disk drives. As shown in Fig. 1, a typical MTJ represents a nanoscale multilayered structure composed of the free layer and pinned layer (FL and PL, respectively). The PL is composed of two antiferromagnetically coupled layers (PL1 and PL2) to reduce the stray field from the PL onto the FL. The antiferromagnetic (AFM) layer fixes the magnetization orientation of the PL1 via the direct exchange coupling between the AFM and PL1. The side bias field keeps the FL magnetization orthogonal to the PL. The stack's shape is tapered to increase the FL's magnetic stability. The magnetization direction of the PL is assumed to be perfectly fixed, while that of the FL rotates in response to the field from the magnetic media. The change in the relative orientation

between the FL and PL magnetizations translates into variations in the sensor's tunnel magnetoresistance (TMR) that indicate the difference between the "up" and "down" bits representing the recorded information [1,2].

MTJs are nonlinear dynamic systems. At room temperature, thermal fluctuations result in random magnetization dynamics of both the FL and PL, which can be quantified by their ferromagnetic resonance (FMR) modes [3]. Another source of magnetization dynamics in MTJs is the spin-torque (ST) effect, which describes a direct transfer of angular momentum from the spin-polarized electrons to the local magnetization [4]. Even in the macrospin approximation, magnetization dynamics are inherently nonlinear because oscillations of magnetization components arise from the precession of the magnetization vector with a constant magnitude, leading to the following nonlinear relation between these components: $m_x^2 + m_y^2 + m_z^2 = 1$ [5]. ST-induced magnetization dynamics result in large-angle magnetization precession where the nonlinear nature of magnetization dynamics becomes especially pronounced.

*auerbach@ifp.tuwien.ac.at

†d.berkov@general-numeric-rl.de

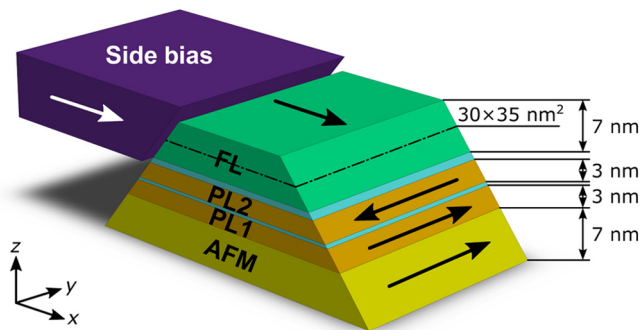


FIG. 1. Structure of a state-of-the-art magnetic tunnel junction (MTJ) used in hard disk drives (see text for details). Arrows represent the average magnetization directions of magnetic layers. The right side bias magnet is not shown.

The fundamental theory of nonlinear oscillations states that their nonlinearity results in new resonances such that oscillations of frequency close to f_0 (natural frequency) can be excited by an external force with a frequency considerably different from f_0 . Namely, a resonant condition might occur at every excitation frequency pf_0/q , where p and q are positive integers. In practice, however, p and q should be small because the resonance strength rapidly decreases with increasing order of nonlinearity [6].

Specific cases of forced oscillations in nonlinear systems excited at nf_0 and f_0/n , where n is a positive integer, are called harmonic (or superharmonic) and subharmonic injection locking, respectively. Injection locking is observed in numerous types of physical systems. Most often, however, this term is associated with electronic oscillators and laser resonators. In optics, injection locking has been used to improve the frequency stability of lasers and reduce the frequency noise of laser diodes. In electronic systems, injection locking has been used to increase the pull-in (or “capture”) range and reduce the output phase jitter in phased-locked loops [7].

In ST-driven systems, e.g., spin-torque nano-oscillators (STNOs), super- and subharmonic injection locking can be used to generate microwave and millimeter wave signals. In Ref. [8], Keatley *et al.* excited dc-biased spin-torque vortex oscillators (STVOs) with an ac signal at multiples (harmonics) of their fundamental frequency. The response was measured at a fractional frequency of the excitation signal corresponding to the fundamental frequency. In Ref. [9], Lebrun *et al.* presented an experimental study of both super- and subharmonic injection locking to an ac excitation signal in dc-biased STVOs. It resulted in pure phase locking with no phase slips and an output power of $>1 \mu\text{W}$ observed at room temperature and zero magnetic field. In Ref. [10], Carpenteri *et al.* performed a numerical study of both super- and subharmonic injection locking in STNOs based on hybrid spin valves composed of two FLs and

orthogonal PLs. In Ref. [11], Quinsat *et al.* reported the results of a comprehensive synthesis of experimental and numerical studies of the superharmonic injection locking in STNOs. This work was inspired by the analytical theory of fractional synchronization presented in Ref. [12], which, in turn, concluded that for large ac power levels, the coupling between the oscillating magnetic layer and the source becomes nonlinear, resulting in a fractional synchronization regime [13].

In this work, we study the subharmonic injection locking in MgO-based MTJs. Combining the nonlinear vector network analyzer (NVNA) measurements and micromagnetic simulations, we show that this locking is determined not only by the intrinsic nonlinearity of the magnetization dynamics, but also by the magnetodipolar feedback between the FL and PL. Furthermore, we demonstrate that the orthogonality of magnetization directions of the FL and PL1 also plays an important role, facilitating the read sensors’ response at $1/2$ the FL FMR frequency f_{FL} . We observe distinct peaks in the dc response at $1/2$, $1/3$, $1/4$, and $1/6$ of f_{FL} . Performing corresponding simulations, we show that these resonances are due to the combination of the low-order nonlinearity, magnetodipolar feedback, and the mutual ST effect between the FL and PL1. Importantly, strong magnetodipolar feedback permits subharmonic injection locking within a wide range of integer fractions of f_{FL} .

The presented work suggests that NVNA measurements in conjunction with micromagnetic modeling can greatly assist in clarifying the uncertainty in defining the system’s magnetic and ST parameters. Furthermore, such a synthesis of nonlinear measurements and modeling identifies the need to consider mutual ST between the FL and PL in micromagnetic modeling.

II. NONLINEAR CHARACTERIZATION

We use the advances in microwave measurement techniques to determine the read sensors’ dc and harmonic responses, which comprise nonlinear characterization. Because of the broadband nature of and variability in the gigahertz-range FMR in read sensors, the nonlinear characterization is performed over a wide frequency range (the excitation frequency ranging from 1 to 15 GHz). Additionally, because of the presence of magnetic shields and bias magnets (Fig. 1), our samples are unsuitable for characterization with an applied magnetic field. The shields would distort the external field such that one would be unable to control the relative orientation of the FLs and PLs to the degree required for such studies. Therefore, all measurements presented in this work are performed without an applied magnetic field, and the excitation is a combination of ac power and dc bias current.

A. dc response

We start with the definition of the voltage induced in the read sensor, which is subjected to both dc and ac currents:

$$I = I_{dc} + I_{ac} \sin(\omega t). \quad (1)$$

In the presence of the TMR effect, the system's resistance has two constituents: magnetization-independent ohmic resistance R_0 and magnetization-dependent, TMR-caused resistance $R_{TMR}(t)$. Hence, the resultant time-dependent voltage response is

$$V(t) = I(t)R(t) = [I_{dc} + I_{ac} \sin(\omega t)] \times [R_0 + R_{TMR}(t)]. \quad (2)$$

If I_{dc} is less than the critical current above which the ST-induced steady-state oscillations arise, the only excitation present in the system is the periodic ac current. Thus, the time-dependent magnetization resulting in the time-dependent TMR term is a periodic function with a period $T = 2\pi/\omega$. Because of various sources of nonlinearities in the system, the TMR-caused resistance can be nonharmonic and subsequently expressed as a Fourier series:

$$R_{TMR}(t) = R_{TMR}^{av} + \sum_{n=1}^{\infty} a_n \cos(n\omega t) + \sum_{n=1}^{\infty} b_n \sin(n\omega t), \quad (3)$$

where the Fourier coefficients a_n and b_n have the dimensionality of resistance. The averaged R_{TMR}^{av} is determined by the nonlinearity of the magnetization oscillations and is highly sensitive to ST asymmetry. This issue is discussed in more detail in Sec. IV. Substituting Eq. (3) into Eq. (2) and then time-averaging the result produces the following dc voltage response:

$$V_{dc} = \langle V(t) \rangle = \underbrace{I_{dc}R_0 + I_{dc}R_{TMR}^{av}}_{\text{"constant"}} + \underbrace{I_{ac} \frac{b_1}{2}}_{\text{"oscillating"}}, \quad (4)$$

where all other higher-order terms disappear after time averaging due to the orthogonality properties of harmonic functions.

In Eq. (4), the “constant” term comes from the magnetization-independent (ohmic resistance) and time-averaged magnetization-dependent, TMR-caused resistances. The “oscillating” term involves mixing the excitation signal with the TMR oscillations only at the same frequency [14]. From Eq. (4), it can also be seen that the contribution from the oscillating term depends on the phase difference $\Delta\phi$ between these two signals: its magnitude is at its maximum at $\Delta\phi = 0^\circ$ or 180° (in or out of phase) and its minimum at $\Delta\phi = 90^\circ$ or 270° (quadrature).

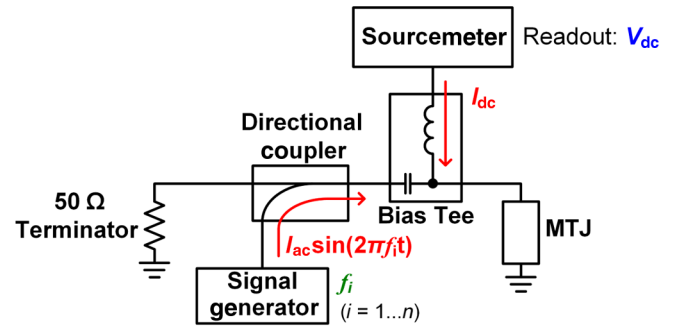


FIG. 2. dc readout ferromagnetic resonance (FMR) measurement relying on the spin-torque (ST) rectification phenomenon.

In this study, the typical MTJ's dimensions are $30 \times 35 \text{ nm}^2$ in the x - y plane and approximately 25 nm in the z direction. Its resistance-area product and TMR ratio are $0.4 \Omega \mu\text{m}^2$ and 90%, respectively. Experimentally, the sensor's dc response can be extracted using the steady-state dc readout measurement technique [14,15]. In the simplest measurement configuration (Fig. 2), the MTJ-based read sensor is excited with an ac signal for different dc bias currents, while the dc voltage across the sensor is measured with a sourcemeter.

In this study, six Western Digital production read sensors are characterized. The representative sample's dc readout measurements shown in Fig. 3 are obtained using the measurement technique introduced in Fig. 2 (utilizing a Keysight PNA-X N5247A as the ac source). Our main observation is the presence of peaks emerging in the dc readout measurements with nonzero dc bias current at frequencies that are the integer fractions (1/2, 1/3, 1/4, and 1/6) of the FL's resonant precession frequency f_{FL} . A similar observation was made in a micromagnetic study of the current-perpendicular-to-plane (CPP) spin-valve heads under ST excitation [16]. A subsequent study of ST-induced magnetization dynamics in thin magnetic nanoelements demonstrated that nanoelements of a certain size can exhibit splitting of their magnetization precession trajectory into limiting subcycles [17]. In the spectrum, these subcycles corresponded to peaks at frequencies lower than that of the complete motion cycle. In Ref. [17], this regime precedes the state of chaos characterized by strongly inhomogeneous large-angle magnetization precession, which produces chaotic trajectories and an almost continuous spectrum with no distinct FMR peaks. In both micromagnetic studies, however, the state near bifurcation (characterized by the presence of peaks at the fractional frequencies of f_{FL}) was observed in a narrow range of corresponding parameters: applied dc bias currents (2.8–3.6 mA) in Ref. [16] or sizes of nanoelements (40–52 nm) in Ref. [17]. In contrast, we observe peaks at the FL's fractional frequencies in a wide range

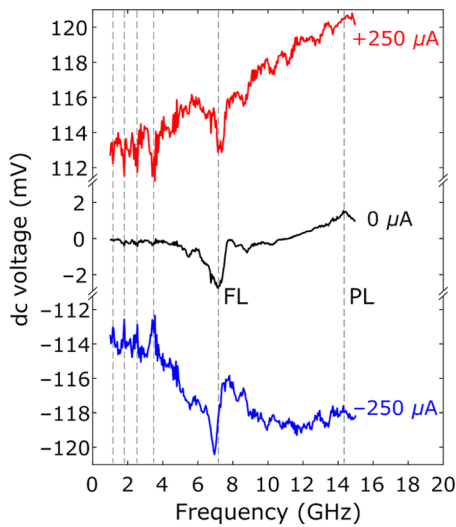


FIG. 3. dc response as a function of the excitation frequency obtained at -5 dBm source power and different dc bias currents. The relatively high excitation level of -5 dBm is selected to emphasize the nonlinear phenomenon. FL and PL denote the free and pinned layers’ natural resonant precession frequencies. (These frequencies are consistent with those obtained with the thermal noise FMR (T-FMR) measurement under the same dc biasing condition.) Positive dc bias corresponds to the electron flow from the PL to FL.

of applied ac and dc signals, which requires an alternative explanation.

B. Harmonic response

The steady-state dc readout measurement technique allows analysis only of the dc spectral component. Since nonlinear effects are involved, a thorough nonlinear harmonic analysis is highly desired. Such an analysis can be accomplished by using a NVNA. Since the characterized magnetic read sensors are one-port devices, this analysis is limited to the one-port scenario.

In contrast to the *linear* VNA, which measures the magnitude ratio and phase difference between the incident and

reflected waves (A_1 and B_1 , respectively) only at the excitation frequency, the NVNA measures the actual A_1 and B_1 waves’ magnitudes and phases at the excitation frequency as well as harmonic components to which energy may be transferred due to the device’s nonlinear characteristics (Fig. 4) [18,19]. In this measurement, the excitation frequency f_i of the incident wave A_1 is swept from 1 to 15 GHz. At each frequency, the fundamental of the reflected wave B_1 is measured at f_i . Naturally, the second harmonic of the reflected wave B_1 is measured at $2f_i$ (2–30 GHz) and the third harmonic is measured at $3f_i$ (3–45 GHz). We emphasize that the resultant measurements represent the frequency response of B_1 , not the power spectrum. A power spectrum is the distribution with frequency of the power content of the signal [20], whereas the frequency response [21] curves in Fig. 5 represent the magnitude of the corresponding harmonic component of B_1 as a function of the excitation frequency and are linearly proportional to voltage.

In Fig. 5, the magnitudes of the fundamental, second, and third harmonics of B_1 are counterposed to the dc readout curve. In Fig. 5(a), the fundamental of B_1 exhibits distinct peaks at frequencies corresponding to f_{FL} , $f_{FL}/2$, $f_{FL}/4$, and (less pronounced) $f_{FL}/6$. These peaks have their counterparts on the dc response curve. In addition, strong peaks are observed in between f_{FL} and $f_{FL}/2$. They might correspond to resonances at frequencies pf_{FL}/q (where p and q are positive integers) and have no analogs in the dc response. Understanding the nature of these additional peaks requires further investigation. In Figs. 5(b) and 5(c), the second and third harmonics of B_1 also reveal distinct peaks at $f_{FL}/2$, $f_{FL}/4$, and (less pronounced) $f_{FL}/6$. Interestingly, the FL mode and the peak located at $f_{FL}/3$ *do not* produce the second and third harmonics of B_1 .

The NVNA measurements imply that the read sensor’s nonlinear characteristics give rise to nonlinear oscillations under the ac excitation signal with the frequency considerably lower than, but still an integer ratio of, the FL mode. Naturally, these dynamics also produce a measurable dc contribution corresponding to this excitation frequency.

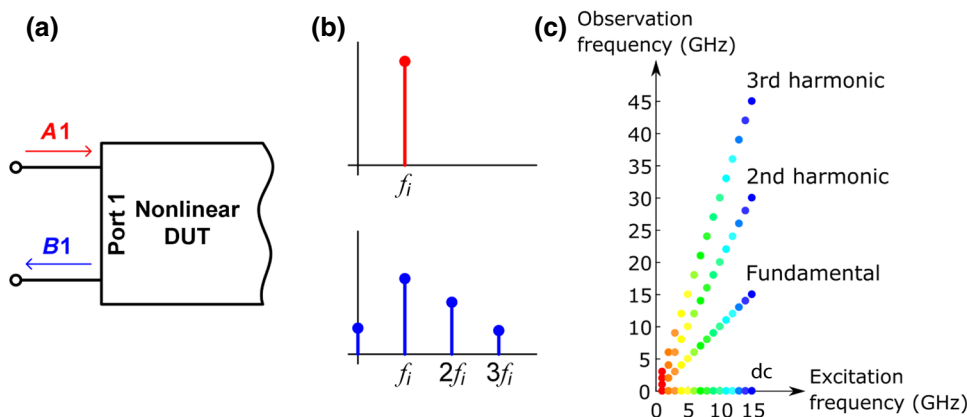


FIG. 4. Nonlinear vector network analyzer (NVNA) measures the incident and reflected waves’ (A_1 and B_1 , respectively) magnitudes and phases (a) at the excitation frequency and at harmonic components (b) to which energy may be transferred due to the device under test’s (DUT’s) nonlinear characteristics. (c) The corresponding excitation and observation frequencies.

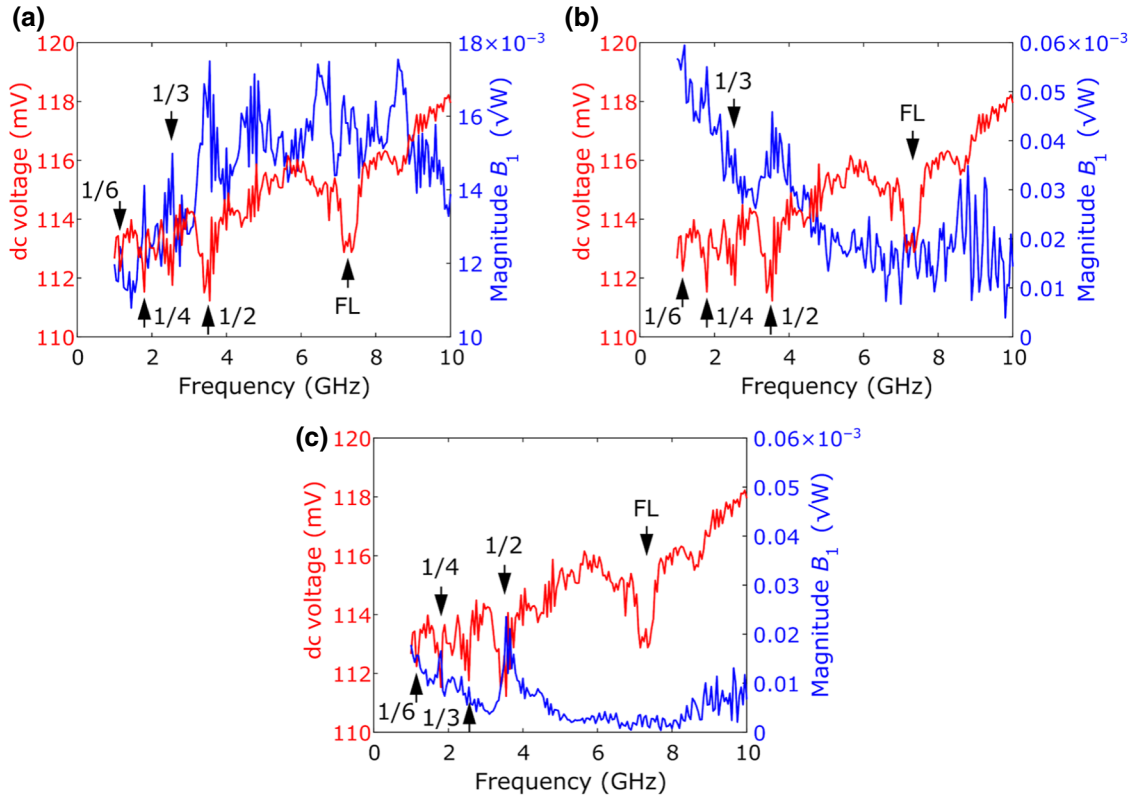


FIG. 5. Representative sample's harmonic response (blue curves) measured with a Keysight PNA-X N5247A at $+250 \mu\text{A}$ dc bias current, -5 dBm ac power, and 15 Hz intermediate frequency bandwidth (IFBW). (a) Fundamental, (b) second, and (c) third harmonics of B_1 plotted versus the excitation frequency. The dc response is shown in red.

III. MICROMAGNETIC MODELING

We employ micromagnetic modeling to understand the underlying physics that enables the dc and harmonic responses at frequencies corresponding to the FL FMR mode's fractional ratios. Because of the model's complexity and uncertainty in the definition of some of its magnetic and ST parameters, we find it vital to discuss in detail the modeling methodology and modeling considerations.

A. Modeling methodology

All numerical simulations presented in this work are performed using the micromagnetic software MicroMagus, which solves the modified Landau-Lifshitz-Gilbert (LLG) equation for the magnetization \mathbf{M} [22],

$$\frac{d\mathbf{M}}{dt} = -\gamma [\mathbf{M} \times (\mathbf{H}_{\text{det}} + \mathbf{H}_{\text{th}})] - \gamma \frac{\lambda}{M_s} \{ \mathbf{M} \times [\mathbf{M} \times (\mathbf{H}_{\text{det}} + \mathbf{H}_{\text{th}})] \}, \quad (5)$$

using one of the optimized Runge-Kutta or Bulirsch-Stoer algorithms with an adaptive step-size control for both $T = 0$ and $T > 0$. In Eq. (5), the precession constant γ is defined via the absolute value of the gyromagnetic ratio γ_0 as $\gamma = \gamma_0 / (1 + \lambda^2)$. The damping constant λ is equal

to the corresponding damping α in the LLG form where the magnetization derivative is present on both sides of the equation.

The deterministic field \mathbf{H}_{det} contains four standard contributions: external, anisotropy, exchange, and magnetodipolar interaction fields. In our case, the ST effect is taken into account via an additional effective field term, which in the standard Slonczewski formalism [23,24] has the form

$$\mathbf{H}_{\text{ST}} = f_J(\theta) [\mathbf{M} \times \mathbf{p}]. \quad (6)$$

Here, the dimensionless ST amplitude f_J depends on the angle θ between the magnetization \mathbf{M} and the spin-polarization direction \mathbf{p} as follows [24,25]:

$$f_J(\theta) = a_J \frac{2\Lambda^2}{(\Lambda^2 + 1) + (\Lambda^2 - 1) \cos \theta}, \quad (7)$$

where the factor a_J is given by

$$a_J = \frac{\hbar}{2|e|} \frac{jP}{M_s^2 d}. \quad (8)$$

In Eqs. (7) and (8), e is the electron charge, j is the electric current density, and d is the thickness of the magnetic layer

subjected to ST. The asymmetry parameter Λ strongly depends on the sample configuration and various transport coefficients [24,25]. When $\Lambda = 1$, the ST effect is assumed to be symmetric. P is the degree of spin polarization of the electrical current [26].

In the LLG equation (5), thermal effects are accounted for by the thermal field term \mathbf{H}_{th} describing random fluctuations induced by the interaction of the ferromagnet with the thermal bath. Components of this fluctuation field have the following statistical properties:

$$\begin{aligned} \langle \mathbf{H}_{\xi,i}^{\text{th}} \rangle &= 0, \\ \langle \mathbf{H}_{\xi,i}^{\text{th}}(0) \mathbf{H}_{\psi,j}^{\text{th}}(t) \rangle &= 2D\delta(t)\delta_{ij}\delta_{\xi\psi}, \end{aligned} \quad (9)$$

meaning that these fluctuations are assumed to be uncorrelated in space and time (i and j are the discretization cell indices; $\xi, \psi = x, y, z$). The noise power D is proportional to the system temperature T :

$$D = \frac{\lambda}{1 + \lambda^2} \frac{kT}{\gamma\mu}. \quad (10)$$

Here, μ is the magnetic moment magnitude of a discretization cell. Unless stated otherwise, all micromagnetic simulations in subsequent sections were performed at $T = 0$ K.

The TMR response introduced in Sec. II A is the quantitative description of the TMR's dependence on the angle θ defined between the magnetizations of adjacent layers [27]:

$$R = \frac{1}{G} = \frac{R_{\perp}}{1 + \frac{\Delta_{\text{TMR}}}{2} \cos \theta}, \quad (11)$$

where R_{\perp} is the sensor resistance at the orthogonal state and Δ_{TMR} is the TMR ratio.

Equation (11) is different from the generally used formulations describing a linear variation of the MTJ's resistance with $\cos \theta$, which appears to be valid only for small values of TMR [27].

B. Modeling considerations

In this study, the MgO-based MTJ devices' PL1, PL2, and FL are made of a similar Co-Fe/Co-Fe-B alloy. The layers' saturation magnetization and exchange stiffness constant are assumed to be $M_s = 1 \times 10^3$ G and $A = 1 \times 10^{-6}$ erg/cm, respectively. The intrinsic Gilbert dampings of the FL and PL2 are set to $\lambda_{\text{FL}} = \lambda_{\text{PL2}} = 0.01$. The IrMn-exchange-pinned damping of the PL1 is initially assumed to be an order of magnitude larger, $\lambda_{\text{PL1}} = 0.1$ [28]. The interlayer coupling strengths are set to values similar to those used in Ref. [29]: $J_1 = 0.04$ erg/cm² between the FL and PL2 ("orange-peel" coupling) and $J_2 = -1.6$ erg/cm²

between the PL1 and PL2 (strong antiferromagnetic coupling via the Ru interlayer).

For each experimental frequency point at a given ac power level and dc bias, we have to perform an independent time-domain micromagnetic simulation. For linear systems that respond only at the excitation frequency, fast broadband excitation can be accomplished via sinc pulses or multifrequency signals (e.g., Schroeder-phased harmonic signals) that are optimal for uniform excitation of all system modes [30,31]. This is done so that, e.g., the ac susceptibility in the whole frequency range of interest can be sampled in a single simulation run. For nonlinear systems, such an approach is not feasible because (1) nonlinear systems respond not only at the excitation frequency but also at its multiples (i.e., harmonics), which strongly interact with each other, and (2) by exciting the system with a strong ST pulse, reaching a dynamic equilibrium state requires significant time, which may be much longer than the duration of the optimal sinc pulse.

To enable faster frequency sweeps around the ranges of interest (i.e., FL FMR frequency and its fractional ratios), the following simplifications to the original read sensor design are adopted. (1) The AFM layer is excluded from simulations, but its effect on the PL1 is taken into account by the corresponding exchange bias field of 1000 Oe [29]. (2) The left and right side bias magnets are also excluded from simulations. Instead, the side bias demagnetizing field is calculated in the quasistatic solver and then included as an external field in all subsequent dynamic simulations. In this model, each magnetic layer is discretized in plane into $N_x \times N_y = 32 \times 20$ cells. No discretization is performed in the out-of-plane direction. We verify that introducing such a discretization even for the thickest layer (i.e., FL) does not lead to any significant changes in final results. With these simplifications, MicroMagus simulations require approximately 1 h to collect 60 ns of magnetization dynamics at $T = 0$ K and approximately 15 h to simulate 200 ns at $T = 300$ K.

To the best of the authors' knowledge, there have not been any comprehensive micromagnetic studies on the nonlinear magnetization dynamics used to predict the MTJ's harmonic response. In general, these dynamics and, by extension, its harmonic response should be sensitive to the various magnetic and ST parameters described above. To test this, we excite the read sensor model via a combination of ac and dc signals (as in the experiment in Fig. 5) at 1/4 the frequency of the FL FMR mode.

1. Effect of the side bias and magnetic shielding

In Fig. 1, the read sensor model is shown without the magnetic shields. In a real system, the top and bottom magnetic shields isolate the sensor from adjacent bits and large writer fields. Material parameters of both shields are typical of permalloy. The shields are sufficiently larger

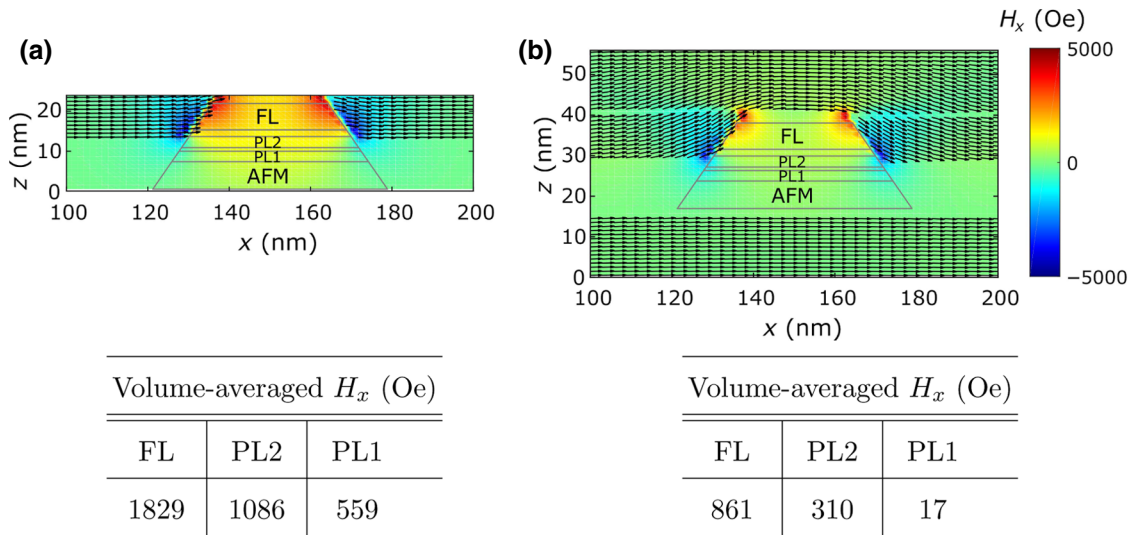


FIG. 6. Simulated side bias field (a) without and (b) with the presence of magnetic shields. The corresponding tables contrast the side bias field onto the free and pinned layers (FL and PL2/PL1, respectively) for these two scenarios. The arrows represent the side bias's and shields' magnetic moments.

than the read sensor. Being unable to micromagnetically model the full-size shields, we reduce their dimensions to $L_x \times L_y \times L_z = 300 \times 36 \times 100 \text{ nm}^3$ and apply the periodic boundary conditions along the x axis to avoid the influence of artificial magnetic “surface charges” from the vertical (in the y - z plane) shield surfaces. By doing this, we estimate the quasiquantitative effect of these shields on the side bias field (Fig. 6).

Figure 6 shows that in the presence of magnetic shields, the simulated side bias field, both onto the FL and especially onto the pinned layers PL2/PL1, sufficiently decreases. This means that the total side bias field (i.e., taking into account the presence of magnetic shields) strongly depends on the shield configuration. Additionally, variations in the spacing between the side bias and the MTJ stack within the fabrication tolerances may affect the side bias field strength. The side bias magnetization is also known to be accurate within approximately $\pm 10\%$. Hence, without having more accurate information concerning the geometry and magnetic parameters of the shields and side bias, we have to adjust the side bias field to match the most reliable experimental results.

The most direct experimental observation is the measured FL FMR frequency. This value can be used to adjust the total external field onto the FL. Based on the obtained value of $f_{\text{FL}} \approx 7 \text{ GHz}$, we determine that the increase in the simulated side bias field onto the FL by a factor of approximately 1.7 is necessary to reproduce this frequency. Moreover, we find that the proposed adjustment of the side bias field onto the FL shifts the system's dynamic regime from quasichaotic toward pure phase locking when excited at fractional frequencies. On one hand, the quasichaotic regime results in a stronger dc response. On the other hand,

this regime is observed only within a narrow range of magnetic and ST parameters and thus is most probably absent in our system. Hence, the quasichaotic regime should be avoided, which also justifies the increase in the FL side bias field.

Adjustment of the side bias field onto the pinned layers PL2/PL1 is a more subtle issue. Here, our main criterion is that the side bias field onto the pinned layers should be such that it allows strongly nonlinear magnetization dynamics, leading to the generation of the higher-order harmonics and the sought-after dc response (Fig. 7). Performing test simulations, we discover that a factor of approximately 0.2 reduction in the simulated side bias field onto the PL2/PL1 is necessary to obtain the measurable dc response and higher-order harmonics.

2. Effect of damping

Another ambiguity is the value of the effective damping λ included in the LLG equation used for simulations. A lower damping constant corresponds to lower power absorption by the magnetic system, consequently leading to nonlinear oscillations with a larger amplitude and, by extension, a stronger harmonic response. While 0.01–0.02 is a typical damping constant for the FL and PL2 [32], the PL1 damping is initially set to a much higher value, $\lambda_{\text{PL1}} = 0.1$ [28]. In Ref. [28], Smith *et al.* suggested the following mechanisms that can explain a factor of 10 increase in the PL standard damping: (1) PL-FL spin pumping and (2) strong interfacial exchange coupling at the IrMn/PL interface.

In test simulations, we observe that the pinned layer PL1 damping strongly affects the read sensor's dynamics

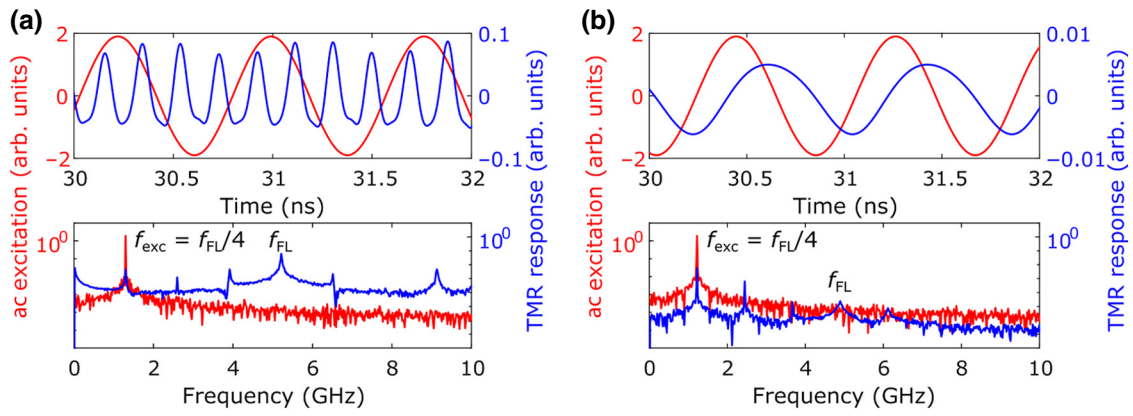


FIG. 7. Time- (top) and frequency-domain (bottom) responses of the read sensor model excited at $1/4$ the free layer (FL) FMR frequency f_{FL} . Lower side bias field onto PL2/PL1 (a) evokes strongly nonlinear magnetization oscillations, accompanied by a stronger harmonic response than in (b). In the amplitude spectra, note the ordinate axes' logarithmic scale. (a) $0.46 \times H_x$. (b) H_x .

(Fig. 8) even though this layer is assumed to be pinned. This effect is due to the large magnetodipolar interaction not only between the PL1 and PL2, but also between the PL1 and FL. The latter interaction is strong because the FL is relatively thick (approximately 7 nm). These couplings lead to a significant energy transfer to the PL1 and substantial energy dissipation resulting from the overdamped dynamics of the PL1. As a consequence, neither a noticeable dc response nor a significant harmonic response is observed at $\lambda_{\text{PL1}} = 0.1$ [Fig. 8(b)].

Based on these observations, we compare the system studied in Ref. [28] with our sensor composition. In contrast to our MTJ-based stack, Smith *et al.* studied current-perpendicular-to-plane giant-magnetoresistive (CPP-GMR) spin-valve stacks. Their samples, being just a pinned layer coupled to an AFM layer, did not have a PL2/PL1 with Ru in between. This can lead to significant differences between the effective dampings of the pinned layer adjacent to the AFM layer in these two systems.

In Ref. [33], Mohammadi *et al.* reported an inverse-thickness-squared dependence of damping for exchange-biased Co-Fe layers and increased damping (but still lower than 0.1 for a 3-nm-thick Co-Fe layer) via spin pumping. Thus, based on the arguments presented above and partially on the results from Ref. [33], we set the PL1 damping constant to the same value $\lambda_{\text{PL1}} = 0.01$ as for other layers. Still, further studies of this question are highly desired.

3. Mutual ST effect between the FL and PL2

Within a multilayered stack, the ST term (6) can be taken into account only on the FL if and only if the following statements are true. (1) The FL is significantly thinner than all other layers. Being a surface effect, the ST is more efficient for thinner layers. (2) The PL is usually pinned to the AFM layer by an exchange-bias coupling, which is much stronger than the external field onto the FL.

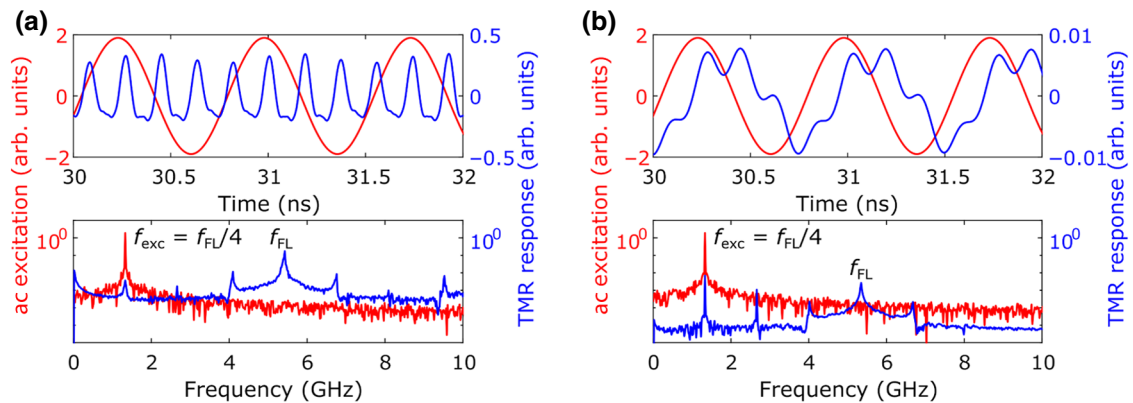


FIG. 8. Time- (top) and frequency-domain (bottom) responses of the read sensor model excited at $1/4$ the FL FMR frequency f_{FL} . Lower pinned layer PL1 damping (a) evokes strongly nonlinear magnetization oscillations, accompanied by a much stronger harmonic response than in (b). In the amplitude spectra, note the ordinate axes' logarithmic scale. (a) $\lambda_{\text{PL1}} = 0.01$. (b) $\lambda_{\text{PL1}} = 0.1$.

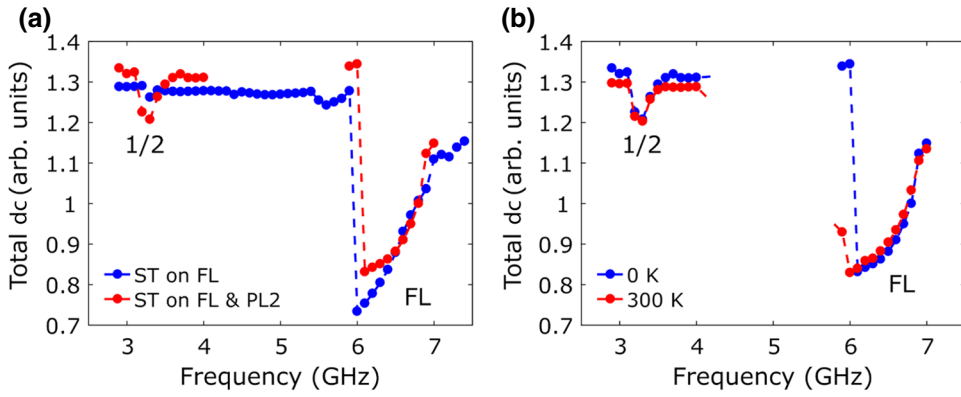


FIG. 9. (a) Simulated dc responses ($\Lambda = 4$, $P = 0.45$) emphasizing the importance of the ST effect not only on the FL but also on the PL2. The corresponding constant and oscillating contributions to the total dc responses are shown in the Appendix, Fig. 16. (b) Simulated dc response for $\Lambda = 4$, $P = 0.45$, and different temperature conditions.

In our case, both statements are false. In the read sensor design, the FL is much thicker than the PL1 (7 nm vs 3 nm). Furthermore, the external (side bias) field onto the FL is approximately the same as the exchange bias field onto the PL1, which is antiferromagnetically coupled to the PL2 (both fields are approximately 1000 Oe). Thus, the FL-PL2 coupling must be considered in any adequate treatment of magnetization dynamics in the read head system. To account for this interaction, we include the ST terms (6) on *both* PL2 and FL. The direction of the electron polarization used to compute the ST effect on the FL is adjusted based on the magnetization direction of the PL2, and vice versa. The ST parameters Λ and P are set to be the same for both layers.

Test simulations confirm the importance of the mutual ST effect between the FL and PL2 [Fig. 9(a)]. In the presence of the ST effect on the PL2, the peak at $f_{\text{FL}}/2$ is ≈ 5 times larger (red dots) than when it is absent (blue dots). The influence of the mutual ST effect is especially pronounced in the dc response's constant term [Fig. 16(a) in the Appendix].

4. Stability of the dynamic regime with respect to thermal fluctuations

Nonlinear dynamic systems are prone to chaotic behavior [34]. In our model, e.g., we achieve a quasichaotic regime when the side bias field onto the FL is too low. Hence, it is necessary to verify the stability of the phase-locking regime with respect to thermal fluctuations. We accomplish this by comparing the simulated dc responses obtained at zero temperature and $T = 300$ K. Figure 9(b) shows that room-temperature fluctuations do not disturb the phase-locking regime and allow the peak at $f_{\text{FL}}/2$ to remain intact.

IV. RESULTS AND DISCUSSION

The micromagnetic modeling considerations proposed in Sec. III B help to calibrate the model. The next step is to relate the simulated dc and harmonic responses to the experimental ones.

To aid the reader, in Fig. 10, we show the representative sample's experimental dc response (extracted from Fig. 3) limited to the frequency range from $f_{\text{FL}}/2$ to f_{FL} (f_{FL} being the FL's natural FMR frequency).

A. dc response

1. Effect of the ST parameters

The spin-torque parameters appear naturally in the derivation of Slonczewski's approximation for asymmetric ferromagnetic-nonferromagnetic-ferromagnetic multilayers [35]. Experiments and theory have provided estimated values for both P and Λ [25,36,37]. Because of the uncertainty in both parameters, $P = 0.35$ and $\Lambda = 1.5$ are only first estimates.

The uncertainty in the ST parameters provides the main degree of freedom in achieving sufficient qualitative agreement between the experimental and simulated dc responses. The characteristic “foldover” FL FMR profiles evolve with increasing spin polarization factors P and asymmetry parameters Λ (Fig. 11). Moreover, higher P and Λ significantly broaden the FL mode's linewidth. We estimate our samples' ST parameters by matching the FL mode's linewidths in the experimental and simulated dc responses. The approximate 0.5-GHz experimental

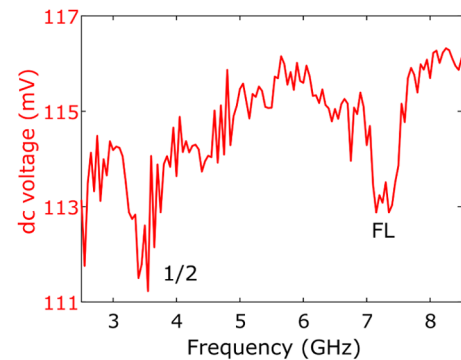


FIG. 10. Experimental dc response shown within the frequency range from $f_{\text{FL}}/2$ to f_{FL} . Its NVNA measurements are presented in Fig. 5.

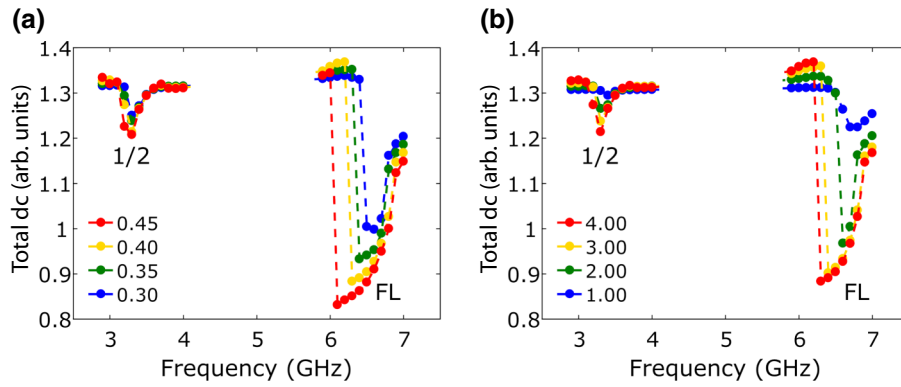


FIG. 11. Simulated dc responses for different (a) spin polarization factors P at $\Lambda = 4$ and (b) asymmetry parameters Λ at $P = 0.4$ plotted versus the excitation frequency. The corresponding constant and oscillating contributions to the total dc responses are shown in the Appendix, Figs. 14 and 15.

linewidth corresponds to $P = 0.4$ and $\Lambda = 4$. These values are higher than our first estimates provided in the published works: $P = 0.35$ and $\Lambda = 1.5$. Such an increase, however, is necessary to match the experimental FL mode's linewidth along with achieving the measurable dc response at $f_{\text{FL}}/2$.

When excited around a fractional frequency of the FL mode, increasing ST parameters facilitate the strongly nonlinear magnetization dynamics accompanied by the generation of the higher-order harmonics and measurable dc [e.g., as in Fig. 8(a)]. The two contributions to the total dc response contain additional physical insights. Figures 14 and 15 in the Appendix show that the dc response at the FL FMR frequency is primarily determined by mixing of the TMR oscillations with the excitation signal [the oscillating term in Eq. (4)]. On the other hand, the dc response at $1/2$ the frequency of the FL FMR mode is defined by the constant term.

2. Response at the FL mode's subharmonics

The magnetodipolar interaction between the FL and PL2 causes positive feedback, which qualitatively affects the system dynamics. This feedback can be thought of as follows. The deviation of the FL magnetization from its preferred orientation generates a stray field. This field causes the PL2 magnetization to deviate in the direction

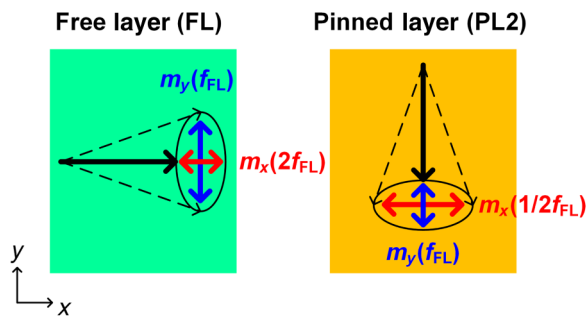


FIG. 12. Magnetization precession's elliptical trajectory and magnetodipolar feedback between the FL and PL2 facilitate the response at $1/2$ the FL frequency.

opposite to that of the FL. This, in turn, results in an even larger deviation of the FL magnetization due to the influence of the PL2 stray field, thus producing positive feedback between the magnetization dynamics of the FL and PL2 [38].

The FL precession exhibits an elliptical trajectory. Thus, the m_x component moves back and forth twice during one oscillation cycle; its oscillation frequency is approximately twice that of the m_y component [39]. If f_{FL} is the FL's resonant precession frequency, then $f(m_x) = 2f(m_y) = 2f_{\text{FL}}$. In this physical picture, the magnetodipolar interaction induces coupling between the FL and PL2. Because of the large y component of the FL's stray field induced by strong m_y oscillations with the frequency f_{FL} , the above-mentioned coupling induces the m_y oscillations of the PL2 with the same frequency f_{FL} . These oscillations, in turn, result in the m_x oscillations of the PL2 with the frequency $f_{\text{FL}}/2$ (Fig. 12). The feedback via the PL2's magnetodipolar field leads to the oscillation of the FL with the frequency $f_{\text{FL}}/2$ as well as all its harmonics. Thus, the FL power spectrum would contain the FL mode, its subharmonic at $f_{\text{FL}}/2$, and their higher-order modes, all of which are produced due to the nonlinear nature of the FL's m_y oscillations and the contribution of the PL2's m_x and m_y oscillations excited by the presence of the magnetodipolar interaction.

Therefore, to facilitate the dc response at $1/2$, $1/3$, $1/4$, and $1/6$ the frequency of the FL FMR mode, it is enough to combine the magnetodipolar feedback between the FL and PL2 with a low-order nonlinearity. The dc response at $1/5$ the frequency of the FL FMR mode is not present in the measurement: it requires a fifth-order nonlinearity, but the fifth harmonic is usually too small to evoke phase locking.

B. Harmonic response

Figure 13 shows the fundamental and second harmonic of TMR counterposed to the total dc response. Whereas the TMR response at $1/2$ the FL FMR frequency f_{FL} has a weak fundamental and a strong second harmonic, the TMR response at the FL FMR frequency has a strong fundamental and a weak second harmonic.

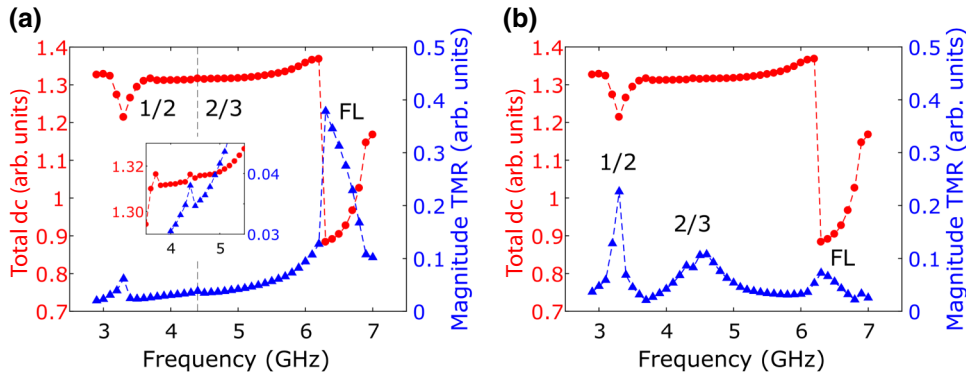


FIG. 13. Simulated TMR response at (a) the excitation frequency (fundamental) and (b) its second harmonic plotted versus the excitation frequency for $\Lambda = 4$ and $P = 0.4$. The presence of peaks corresponding to $2/3$ the FL FMR frequency f_{FL} suggests that the resonant condition might occur at excitation frequencies other than f_{FL}/n , where n is a positive integer.

The former observation implies that the MTJ's nonlinear characteristics give rise to nonlinear oscillations under the ac excitation signal with the frequency corresponding to $1/2$ the FL natural precession frequency. As the TMR response at the second harmonic is stronger than at the fundamental, the FL FMR mode seems to phase lock to this harmonic. As for the latter observation, the FL FMR mode phase locks to the TMR oscillations at the excitation frequency, thus producing a strong fundamental at the FL FMR frequency.

The major discrepancy between the measurements in Figs. 5(a) and 5(b) and simulations in Fig. 13 is the absence of the strong fundamental of B_1 at the FL FMR frequency f_{FL} . We attribute this difference to weak coupling (because of the convergence to steady-state phase locking) between the NVNA's incident wave and magnetization precession. We suggest that the experimental magnetization precession has a less stable phase relation with the NVNA's incident signal than in the model.

In Fig. 5(a), the ripply response in the fundamental of B_1 suggests that there are more peaks at fractional frequencies of the FL mode than what we identify. In particular, the enlarged dc responses in Fig. 10 indicate a resonant feature between $1/2$ the FL FMR mode and the FL FMR mode. We qualitatively replicate this feature in the simulated TMR response [Figs. 13(a) (inset) and 13(b)]. Contrary

to the experiment, however, the FL FMR mode seems to phase lock to the second harmonic, not to the TMR oscillations at the excitation frequency corresponding to $2/3$ the FL FMR frequency f_{FL} . This is clearly seen in the time- and frequency-domain TMR responses for two selected excitation frequencies: $2/3$ the frequency of the FL FMR mode and 5 GHz (Fig. 17 in the Appendix). The magnetic system's harmonic response (specifically, of the second harmonic) is stronger if the excitation frequency corresponds to a fractional frequency of the FL FMR mode.

V. CONCLUSION

We discover that all characterized magnetic sensors' dc responses reveal peaks at frequencies that are the integer fractions ($1/2$, $1/3$, $1/4$, and $1/6$) of the devices' natural FL FMR frequency f_{FL} . These peaks, in turn, generate the corresponding second and third harmonics of B_1 . To understand the underlying physics that enabled the dc response at subharmonics of the FL mode, we employ micromagnetic modeling.

A comprehensive micromagnetic study suggests that the experimentally observed dc response at $1/2$, $1/3$, $1/4$, and $1/6$ of f_{FL} can be defined by a low-order nonlinearity and strong magnetodipolar feedback between the FL and PL. As the PL is significantly thinner than the FL,

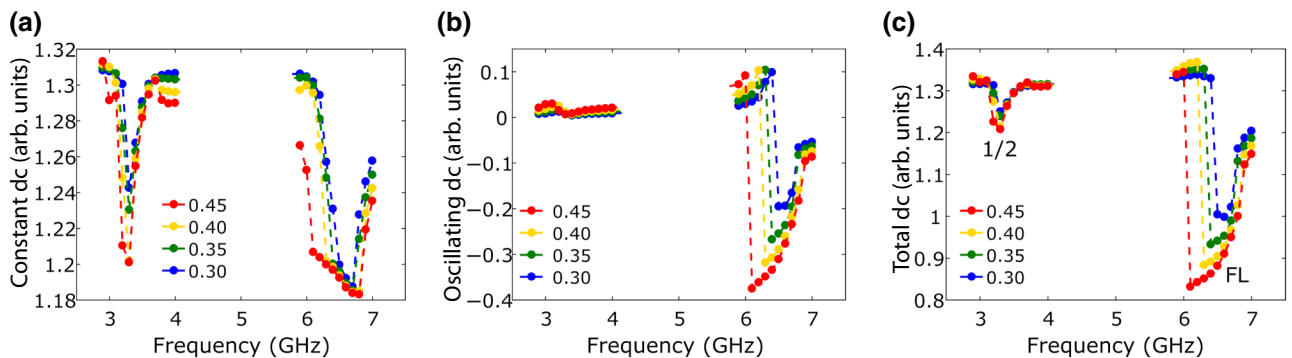


FIG. 14. Simulated (a) constant and (b) oscillating contributions to (c) the total dc response for different spin polarization factors P at $\Lambda = 4$.

additionally accounting for the ST effect on this layer notably enhances the ST-driven harmonic response. Interestingly, the orthogonality of the FL and PL also facilitate the magnetic sensors' response at 1/2 the FL FMR frequency f_{FL} .

Most importantly, strong magnetodipolar feedback permits subharmonic injection locking within a wide range of integer fractions, which can be used in the development of a new generation of frequency multipliers.

ACKNOWLEDGMENTS

E.A. and D.B. gratefully appreciated financial support from the Deutsche Forschungsgemeinschaft (Research Project No. BE 2464/18-1).

APPENDIX

This appendix summarizes the effect of ST parameters on the read sensor's dc response.

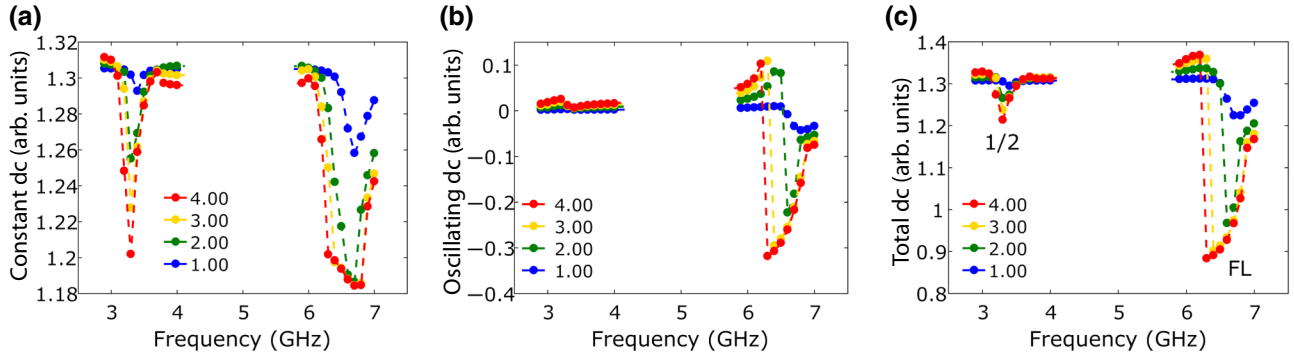


FIG. 15. Simulated (a) constant and (b) oscillating contributions to (c) the total dc response for different asymmetry parameters Λ at $P = 0.4$.

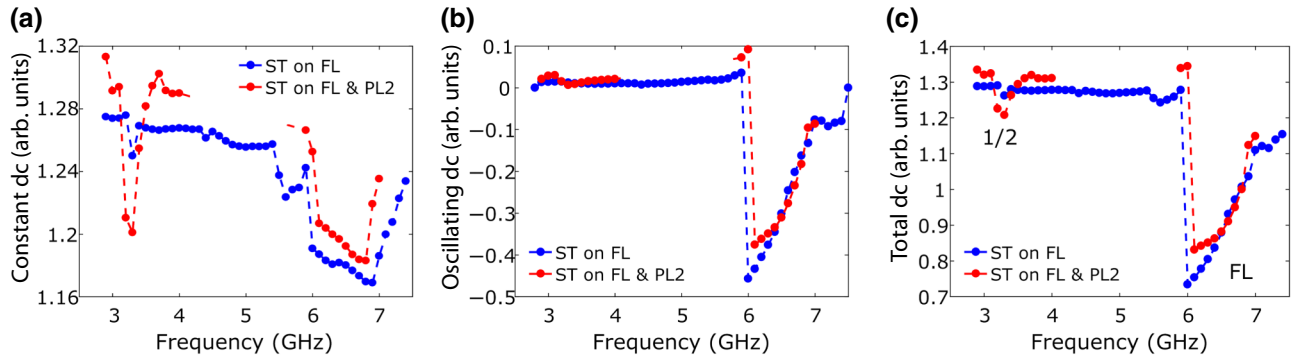


FIG. 16. Simulated (a) constant and (b) oscillating contributions to (c) the total dc response for $\Lambda = 4$, $P = 0.45$, and different ST scenarios.

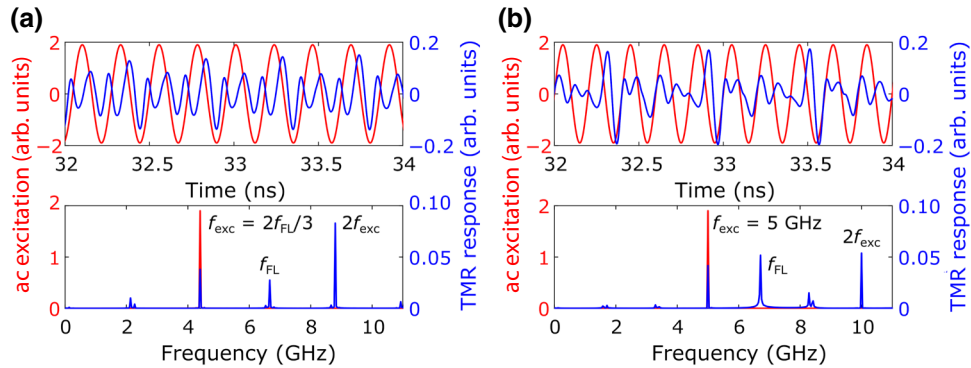


FIG. 17. Time- (top) and frequency-domain (bottom) responses of the read sensor model excited at (a) 2/3 the FL FMR frequency f_{FL} and (b) 5 GHz. The magnetic system's harmonic response (specifically, of the second harmonic) is stronger if the excitation frequency corresponds to a fractional frequency of the FL FMR mode.

- [1] J.-G. Zhu and Chando Park, Magnetic tunnel junctions, *Mater. Today* **9**, 36 (2006).
- [2] J. Heidmann and A. M. Taratorin, in *Handbook of Magnetic Materials*, edited by K. H. J. Buschow (Elsevier, Amsterdam, Netherlands, 2011), 1st ed., Vol. 19, Chap. 1, p. 1.
- [3] C. Kittel, Ferromagnetic resonance, *J. Phys. Radium* **12**, 291 (1951).
- [4] A. Brataas, A. D. Kent, and H. Ohno, Current-induced torques in magnetic materials, *Nat. Mater.* **11**, 372 (2012).
- [5] D. V. Berkov and J. Miltat, Spin-torque driven magnetization dynamics: Micromagnetic modeling, *J. Magn. Magn. Mater.* **320**, 1238 (2008).
- [6] L. D. Landau and E. M. Lifshitz, *Course of Theoretical Physics: Mechanics* (Butterworth-Heinemann, Oxford, UK, 1976), 3rd ed., Chap. 29, p. 87.
- [7] P. Maddaloni, M. Bellini, and P. D. Natale, *Laser-Based Measurements for Time and Frequency Domain Applications: A Handbook* (CRC Press, Boca Raton, FL, USA, 2013), Chap. 2.6.2, p. 76.
- [8] P. S. Keatley, S. R. Sani, G. Hrkac, S. M. Mohseni, P. Dürrenfeld, J. Åkerman, and R. J. Hicken, Superharmonic injection locking of nanocontact spin-torque vortex oscillators, *Phys. Rev. B* **94**, 094404 (2016).
- [9] R. Lebrun, A. Jenkins, A. Dussaux, N. Locatelli, S. Tsunegi, E. Grimaldi, H. Kubota, P. Bortolotti, K. Yakushiji, J. Grollier, A. Fukushima, S. Yuasa, and V. Cros, Understanding of Phase Noise Squeezing under Fractional Synchronization of a Nonlinear Spin Transfer Vortex Oscillator, *Phys. Rev. Lett.* **115**, 017201 (2015).
- [10] M. Carpentieri, T. Moriyama, B. Azzerboni, and G. Finocchio, Injection locking at zero field in two free layer spin-valves, *Appl. Phys. Lett.* **102**, 102413 (2013).
- [11] M. Quinsat, J. F. Sierra, I. Firastrau, V. Tiberkevich, A. Slavin, D. Gusakova, L. D. Buda-Prejbeanu, M. Zarudniev, J.-P. Michel, U. Ebels, B. Dieny, M.-C. Cyrille, J. A. Katine, D. Mauri, and A. Zeltser, Injection locking of tunnel junction oscillators to a microwave current, *Appl. Phys. Lett.* **98**, 182503 (2011).
- [12] S. Urazhdin, P. Tabor, V. Tiberkevich, and A. Slavin, Fractional Synchronization of Spin-torque Nano-oscillators, *Phys. Rev. Lett.* **105**, 104101 (2010).
- [13] A. Dussaux, A. V. Khvalkovskiy, J. Grollier, V. Cros, A. Fukushima, M. Konoto, H. Kubota, K. Yakushiji, S. Yuasa, K. Ando, and A. Fert, Phase locking of vortex based spin transfer oscillators to a microwave current, *Appl. Phys. Lett.* **98**, 132506 (2011).
- [14] J. C. Sankey, P. M. Braganca, A. G. F. Garcia, I. N. Krivorotov, R. A. Buhrman, and D. C. Ralph, Spin-transfer-driven Ferromagnetic Resonance of Individual Nanomagnets, *Phys. Rev. Lett.* **96**, 227601 (2006).
- [15] A. A. Tulapurkar, Y. Suzuki, A. Fukushima, H. Kubota, H. Maehara, K. Tsunekawa, D. D. Djayaprawira, N. Watanabe, and S. Yuasa, Spin-torque diode effect in magnetic tunnel junctions, *Nature* **438**, 339 (2005).
- [16] J.-G. Zhu and X. Zhu, Spin transfer induced noise in CPP read heads, *IEEE Trans. Magn.* **40**, 182 (2004).
- [17] D. Berkov and N. Gorn, Transition from the macrospin to chaotic behavior by a spin-torque driven magnetization precession of a square nanoelement, *Phys. Rev. B* **71**, 052403 (2005).
- [18] P. Roblin, *Nonlinear RF Circuits and Nonlinear Vector Network Analyzers* (Cambridge University Press, Cambridge, UK, 2011), 1st ed.
- [19] K. A. Remley, in *Proc. 73rd ARFTG Microwave Measurement Conference* (IEEE, 2009), p. 1.
- [20] R. B. Randall, *Frequency analysis* (Brüel & Kjær, Nærum, Denmark, 1987), 3rd ed., Chap. 2.2.1, p. 23.
- [21] R. E. Ziemer and W. H. Tranter, *Principles of Communications: Systems, Modulation, and Noise* (John Wiley & Sons Ltd., USA, 2014), 7th ed., Chap. 2.6.4, p. 201.
- [22] D. V. Berkov and N. L. Gorn, Micromagus: Package for micromagnetic simulations, <http://www.micromagus.de>.
- [23] J. C. Slonczewski, Current-driven excitation of magnetic multilayers, *J. Magn. Magn. Mater.* **159**, L1 (1996).
- [24] J. C. Slonczewski, Currents and torques in metallic magnetic multilayers, *J. Magn. Magn. Mater.* **247**, 324 (2002).
- [25] J. Xiao, A. Zangwill, and M. D. Stiles, Boltzmann test of Slonczewski's theory of spin-transfer torque, *Phys. Rev. B* **70**, 172405 (2004).
- [26] To describe the ST's angular dependence in MgO-based junctions, we used the common formulations for metallic junctions. Recent work (Ref. [40]) shows that the effective difference in angular dependence for these two scenarios is insignificant.
- [27] H. Jaffrès, D. Lacour, F. N. Van Dau, J. Briatico, F. Petroff, and A. Vaurès, Angular dependence of the tunnel magnetoresistance in transition-metal-based junctions, *Phys. Rev. B* **64**, 064427 (2001).
- [28] N. Smith, M. J. Carey, and J. R. Childress, Measurement of Gilbert damping parameters in nanoscale CPP-GMR spin valves, *Phys. Rev. B* **81**, 184431 (2010).
- [29] M. Pauselli, A. Stankiewicz, Y. Zhang, and G. Carlotti, Magnetic noise and spin-wave eigenmodes in a magnetic tunnel junction read head, *IEEE Trans. Magn.* **53**, 4400606 (2017).
- [30] M. R. Schroeder, Synthesis of low-peak-factor signals and binary sequences with low autocorrelation, *IEEE Trans. Inf. Theory* **16**, 85 (1970).
- [31] E. Van der Ouderaa, J. Schoukens, and J. Renneboog, Peak factor minimization of input and output signals of linear systems, *IEEE Trans. Ins. Meas.* **37**, 201 (1988).
- [32] N. Smith and P. Arnett, White-noise magnetization fluctuations in magnetoresistive heads, *Appl. Phys. Lett.* **78**, 1448 (2001).
- [33] J. B. Mohammadi, J. M. Jones, S. Paul, B. Khodadadi, C. K. A. Mewes, T. Mewes, and C. Kaiser, Broadband ferromagnetic resonance characterization of anisotropies and relaxation in exchange-biased IrMn/CoFe bilayers, *Phys. Rev. B* **95**, 064414 (2017).
- [34] B. K. Shivamoggi, *Nonlinear Dynamics and Chaotic Phenomena: An Introduction* (Springer, Dordrecht, Netherlands, 2014), 2nd ed.
- [35] J. C. Slonczewski, Currents, torques, and polarization factors in magnetic tunnel junctions, *Phys. Rev. B* **71**, 024411 (2005).
- [36] I. N. Krivorotov, D. V. Berkov, N. L. Gorn, N. C. Emley, J. C. Sankey, D. C. Ralph, and R. A. Buhrman, Large-amplitude coherent spin waves excited by spin-polarized current in nanoscale spin valves, *Phys. Rev. B* **76**, 024418 (2007).

- [37] W. H. Rippard, A. M. Deac, M. R. Pufall, J. M. Shaw, M. W. Keller, S. E. Russek, G. E. W. Bauer, and C. Serpico, Spin-transfer dynamics in spin valves with out-of-plane magnetized CoNi free layers, *Phys. Rev. B* **81**, 014426 (2010).
- [38] D. V. Berkov and N. L. Gorn, Spin-torque driven magnetization dynamics in a nanocontact setup for low external fields: Numerical simulation study, *Phys. Rev. B* **80**, 064409 (2009).
- [39] D. V. Berkov and N. L. Gorn, Magnetization precession due to a spin-polarized current in a thin nanoelement: Numerical simulation study, *Phys. Rev. B* **72**, 094401 (2005).
- [40] E. Kowalska, A. Fukushima, V. Sluka, C. Fowley, A. Kákay, Y. Aleksandrov, J. Lindner, J. Fassbender, S. Yuasa, and A. M. Deac, Tunnel magnetoresistance angular and bias dependence enabling tuneable wireless communication, arXiv:1808.10812 (2018).

Correction: The omission of a support statement in the Acknowledgment section has been remedied.